# Rapid growth of angle-confined large-domain graphene bicrystals

Huaying Ren<sup>1,2</sup>, Huan Wang<sup>1</sup>, Li Lin<sup>1</sup>, Miao Tang<sup>1</sup>, Shuli Zhao<sup>1</sup>, Bing Deng<sup>1</sup>, Manish Kumar Priydarshi<sup>1</sup>, Jincan Zhang<sup>1,2</sup>, Hailin Peng<sup>1</sup> (⋈), and Zhongfan Liu<sup>1</sup> (⋈)

Received: 17 November 2016 Revised: 26 January 2017 Accepted: 13 February 2017

© Tsinghua University Press and Springer-Verlag Berlin Heidelberg 2017

#### **KEYWORDS**

graphene, bicrystal, chemical vapor deposition, surface engineering, grain boundary, heating device

#### **ABSTRACT**

In the chemical vapor deposition growth of large-area graphene polycrystalline thin films, the coalescence of randomly oriented graphene domains results in a high density of uncertain grain boundaries (GBs). The structures and properties of various GBs are highly dependent on the misorientation angles between the graphene domains, which can significantly affect the performance of the graphene films and impede their industrial applications. Graphene bicrystals with a specific type of GB can be synthesized via the controllable growth of graphene domains with a predefined lattice orientation. Although the bicrystal has been widely investigated for traditional bulk materials, no successful synthesis strategy has been presented for growing two-dimensional graphene bicrystals. In this study, we demonstrate a simple approach for growing well-aligned large-domain graphene bicrystals with a confined tilt angle of 30° on a facilely recrystallized single-crystal Cu (100) substrate. Control of the density of the GBs with a misorientation angle of 30° was realized via the controllable rapid growth of subcentimeter graphene domains with the assistance of a cooperative catalytic surface-passivation treatment. The large-area production of graphene bicrystals consisting of the sole specific GBs with a tunable density provides a new material platform for fundamental studies and practical applications.

#### 1 Introduction

Graphene is a two-dimensional (2D) Dirac material that has outstanding electronic and optical properties and is attracting extensive attention. Among the various

graphene synthesis methods, the chemical vapor deposition (CVD) growth of graphene films, especially on Cu substrates, is broadly deemed considered as one of the most practical methods for numerous technological applications [1, 2]. However, the properties

Address correspondence to Zhongfan Liu, zfliu@pku.edu.cn; Hailin Peng, hlpeng@pku.edu.cn



<sup>&</sup>lt;sup>1</sup> Center for Nanochemistry, Beijing Science and Engineering Center for Nanocarbons, Beijing National Laboratory for Molecular Sciences, College of Chemistry and Molecular Engineering, Peking University, Beijing 100871, China

<sup>&</sup>lt;sup>2</sup> Academy for Advanced Interdisciplinary Studies, Peking University, Beijing 100871, China

of graphene are significantly degraded by a high density of uncertain grain boundaries (GBs) [3-5]. The GBs in graphene films are the line defects between two domains with different crystallographic orientations [6, 7]. Atomic imaging reveals that GBs consist of pentagon-heptagon pairs, whose arrangement is defined by the misorientation angles between the two domains [7]. The stability and mechanical and electrical properties of the GBs vary with respect to the atomic arrangement [6–8]. According to theoretical predictions, some GBs of graphene have great potential for use as components of future valleytronic devices [9]. However, these nanodevice prototypes have not been experimentally realized, owing to the absence of fixed-orientation graphene materials. CVD-grown graphene films on Cu foils contain randomly orientated domains, yielding various GBs in the final product [10-12]. Thus, if the orientation of the graphene domains is predefined, graphene films with a desired type of graphene GB can be synthesized. Grains with a two-lattice orientation allow the formation of a material with specific type of GB, i.e., the bicrystal.

The bicrystal has been intensively explored and designed for traditional bulk materials, such as polycrystalline metals [13], metallic alloys [14, 15], and ceramics [16], in order to improve their mechanical performance. For example, by welding two single crystals together face-to-face at predetermined misorientations, hexagonal close-packed (hcp) ZnO bicrystals were prepared [17]. Considering that the boundary plane orientation is influenced by the positioning of the seeds, the misorientation bicrystals of a YBa<sub>2</sub>Cu<sub>3</sub>O<sub>x</sub> (Y123) superconductor were well-controlled via the angle-fixed dual seeding of Nd<sub>1+x</sub>Ba<sub>2-x</sub>Cu<sub>3</sub>O<sub>y</sub> single crystals [18]. Recently, a bicrystal in ultrathin 2D noble metal nanostructures was also reported. A (110)<sub>h</sub>oriented hcp and (100)<sub>f</sub>-oriented face-centered cubic Au bicrystal nanosheet was obtained by the transformation of the initial phase, which was induced by ligand exchange [19]. However, no methods for preparing bicrystals of emerging 2D materials—especially graphene—have been reported.

In contrast to three-dimensional materials, the formation of 2D graphene bicrystals can theoretically be achieved via the controlled growth and coalescence of graphene domains with two crystallographic

orientations along the graphene basal plane. The orientation of graphene domains is mainly affected by the lattice orientation of the underlying substrate [10]. Calculations reveal that the graphene domains on a Cu (100) surface have two equivalent orientations rotated by 30° [20], suggesting a strategy for preparing angle-confined graphene bicrystals. The use of a single-crystal Cu substrate is critical for the growth of graphene monocrystal and bicrystal films. However, commercial Cu single crystals are typically too expensive and too small (<60 mm in diameter) to satisfy the next generation of large-scale graphene products. On the other hand, with regard to industrial production and applications, the commercially available Cu foil for graphene growth is usually polycrystalline, leading to the uncontrollability of the graphene lattice orientation. Recently, we developed a facile method for obtaining an inch-sized Cu (100) single crystal that was rapidly recrystallized from commercial Cu foil with the assistance of O chemisorption-induced reconstruction [21, 22].

Herein, for the first time, we present a simple approach for the rapid growth of angle-confined graphene bicrystals on a Cu (100) substrate reconstructed from polycrystalline Cu foil. The isolated single-crystalline domains were arranged in an array with only two tilt angles (0° or 30° in lattice) on the whole Cu substrate (up to 16 cm<sup>2</sup>), leading to the formation of bicrystals with only one certain GB. For controlling the density of specific GBs, the domain size of graphene was tuned from sub-centimeter (6 mm) to micrometer size. This was realized by catalytic surface-passivation of the active-sites method [23] with a 2-amino-4-methoxy-6-methyl-1,3,5-triazine (AMOMT) compound. In addition, a rational feeding process, together with catalytic surface-passivation treatment, was conducted after the nucleation stage, which was beneficial for increasing the lateral growth rate of the graphene [24, 25]. Applications of the graphene bicrystal film in transparent conductive films and heating devices were demonstrated.

#### Results and discussion

The evolution of the graphene bicrystals is illustrated in Fig. 1(a). First, the well-aligned square-shaped graphene

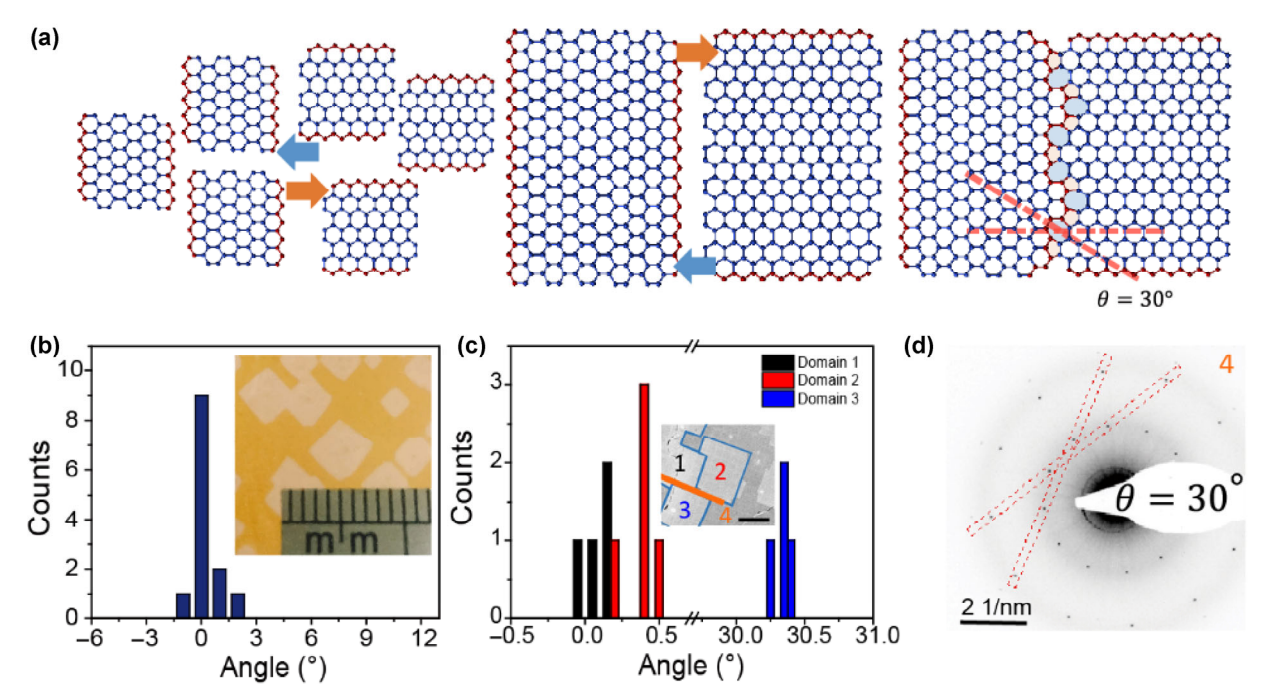


Figure 1 Angle-confined bicrystal. (a) Schematics of the growth process of the bicrystal, showing the relationship between the relative orientations of the adjacent domains. (b) Histogram of the angle distribution of the graphene domains for the sample with a low nucleation density. Inset: a corresponding photograph of 6-mm graphene grains on Cu foil grown by the cooperative passivation approach. Each tick mark represents 1 mm. (c) Histogram of the angle distribution from extensive SAED patterns for different graphene domains shown in the inset. Inset: a SEM image of the as-grown bicrystals transferred onto a TEM grid. The scale bar represents 100 μm. (d) SAED pattern for the orange line shown in the inset of (c), indicating the twist angle of the bicrystal boundary.

single-crystalline domains were grown on Cu foil with a confined twist angle of 0° or 30°. Subsequently, the coalescence of domains with misorientation angle of 30° formed a 0°/30° GB, while the coalescence of domains with no misorientation angle formed a single crystal [26, 27]. To achieve this, before the graphene growth, the vertically stacked Cu foil was pretreated with trace amounts of O for the formation of the single-crystal Cu (100) surface, as reported in our previous work [21]. Note that, cold-rolled Cu foil can provide multi-faceted surfaces for graphene growth [28, 29], while the Cu foil is able to form a large-area Cu (100) surface after annealing for a long time under certain conditions, e.g., O chemisorption [22, 27, 29, 30]. Furthermore, the stacking structure accelerated the crystallographic-texture transformation of the Cu foil (illustrated in Fig. S1(a) in the Electronic Supplementary Material (ESM)). Because the percentage of Cu (100) on the surface increased with the annealing temperature and time [27], the stacking structure provided a confined space, which may

have increased the speed of the evaporation and the redeposition of Cu [31]. This led to the facile formation of a large-area Cu (100) surface with a single rotational domain (Fig. S2 in the ESM). Consequently, the crystallographic texture of the Cu surface after the annealing process was highly sensitive to the fabrication process (for the detailed growth process, see the ESM).

An optical microscopy (OM) image of the as-grown sub-centimeter-sized (6 mm) graphene single-crystal domains is shown in the inset of Fig. 1(b), where the individual graphene domains all exhibit a square shape. This square shape was presumably caused by the symmetry of the underlying Cu (100) substrates [32, 33]. Furthermore, the relative angle distributions across the substrate size, which had an area as large as 20 cm², extracted from the optical images (Fig. 1(b) and Fig. S3 in the ESM) are small. This indicates that the graphene domains were well-aligned with each other across the whole piece of Cu foil, which is easily observed by the naked eye, regardless of the nucleation density of the grains (Fig. S3 in the ESM). The good

alignment of the large single-crystalline graphene domains at the macroscopic level is attributed to the alignment of the Cu atomic steps of Cu (100) in two orthogonal directions. The Cu atomic steps were parallel to the edges of the square graphene domains. These steps were formed by the annealing of the recrystallized cube surface plane edge of Cu, which was parallel to the rolling direction [22]. That is, the alignment of the graphene domains was determined by the initial state of the epitaxial substrate, rather than by the growth parameters.

To confirm the relative orientations between the aligned graphene domains, the graphene film sample was transferred onto a transmission electron microscopy (TEM) grid supported by an amorphous C film, as shown in the scanning electron microscopy (SEM) image in the inset of Fig. 1(c). To characterize the crystallographic orientations of each square domain, the corresponding selected-area electron diffraction (SAED) patterns were obtained for three different domains (marked by numbers in Fig. S4 in the ESM). Domains 1 and 2 exhibited almost the same orientation. Domain 3 had a 30° misorientation angle compared with domains 1 and 2. This is also evident in the SAED patterns for the boundary between domains 1 and 3 (Fig. S4 in the ESM). The histogram of the relative orientations of the different single-crystalline domains extracted from the SAED patterns (Fig. 1(d)) confirms the 30° lattice rotation. For an individual square grain, the two edges of the grain exhibited an armchair geometry, and the other two were zigzag edges. Consequently, a 0°/30° GB was formed when one zigzag edge and one armchair edge merged, whereas no GB was formed when two edges of the same type merged. Thus, graphene bicrystals were successfully formed.

The characterization of the orientation using SAED patterns is limited with regard to the area for detection (typically <3 mm) and requires a tedious transfer process. Consequently, to visualize and evaluate the orientation of the entire large-area sample, facile anisotropic etching treatment was performed after the graphene growth, which was realized by terminating the supply of the precursor and introducing 100 sccm Ar and 20 sccm H<sub>2</sub> for 30 s. Theoretical calculations and experiments revealed that the fastest etching direction was the (2110) direction of the graphene

and that the slowest was  $\langle 10\overline{1}0 \rangle$ , confirming that the zigzag edge was the most stable structure under H<sub>2</sub> etching [34–36]. The nature of the etching anisotropy can be used for visualizing the lattice orientation of the graphene films (Fig. 2(a)). Typical etching results are presented in Fig. 2(b), where hexagonal holes with a lateral size of approximately 1–5 µm formed. The sharp edges of the holes correspond well to the orientation of the square single-crystal domain. Therefore, the relative orientation of the lattice is easily observed by comparing the relative torsional angle of the etching holes with the shape of the square domains. For example, Fig. 2(c) shows three graphene domains that merged together, forming a bicrystal. The hexagonal holes from domain 1 (Fig. 2(d) and Fig. S5 in the ESM) and domain 2 (Fig. 2(e) and Fig. S5 in the ESM) exhibit a 30° rotation, confirming the formation of bicrystals. To identify the graphene orientations over the entire Cu substrate, 50 holes were imaged randomly for a Cu substrate with an area of 16 cm<sup>2</sup> (inset of Fig. 2(f) and Fig. S6 in the ESM). The histogram of the relative misorientation angles is shown in Fig. 2(f), indicating that the graphene domains distributed on the foil exhibited only 0° and 30° rotational angles with occupations of ~54% and ~46%, respectively. However, there are inevitable narrow distributions of the mismatch angles, which resulted from the graphene wrinkles induced during the growth [37-39]. We conclude that the as-formed graphene exhibited only two lattice orientations. Notably, GBs with misorientation angles of 30° are very stable, exhibiting the lowest formation energy [6] and highest strengths [7] compared with GBs having all the other boundary angles, yielding graphene bicrystals with outstanding quality.

In summary, we developed a facile strategy for the rapid growth of large-area angle-confined graphene bicrystals that exhibit only two lattice orientations with a tilt angle of ~30°. An efficient cooperative passivation strategy was developed to suppress the graphene nucleation density using a new passivation compound. A rational precursor-feeding process was used to offset the insufficient C supply during the growth, yielding a high growth rate of 70 μm·min-1 for the sub-centimeter graphene single crystals. A series of characterizations indicated the high quality

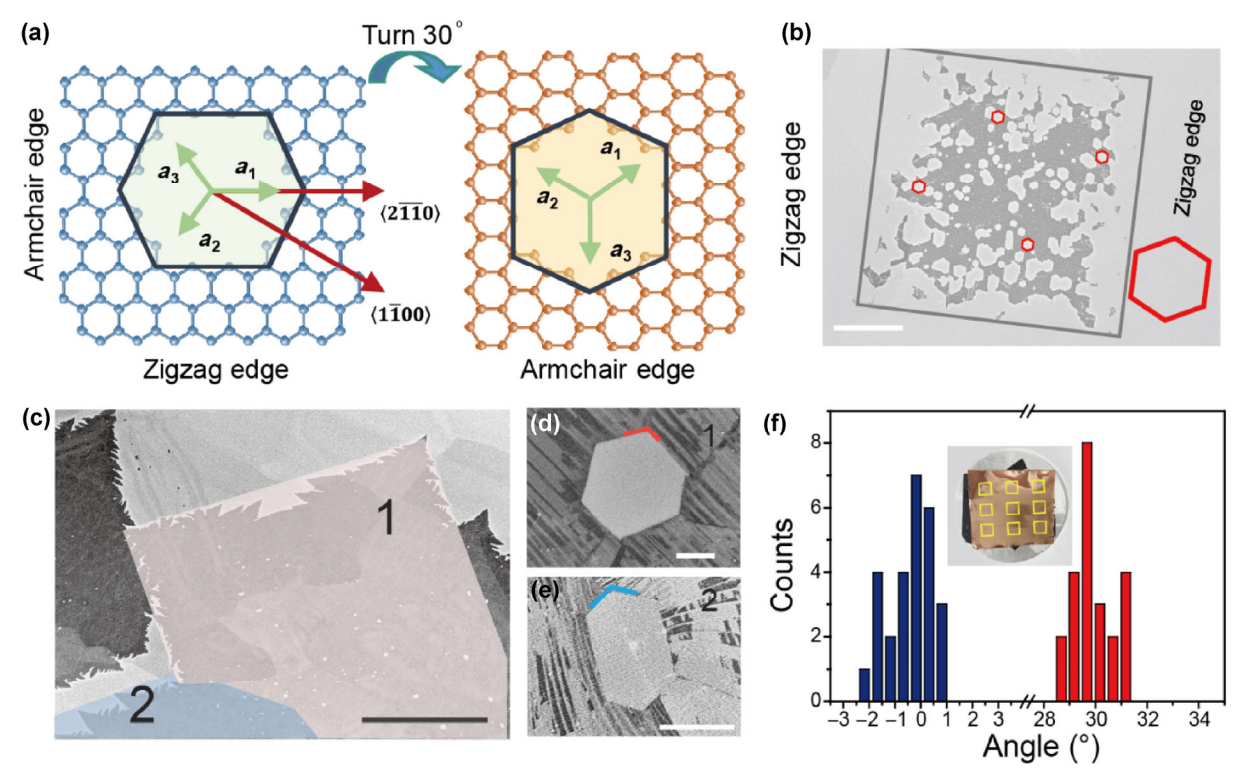


**Figure 2** Large-area characterization for the 30° tilt angle in the lattice of the bicrystal. (a) Schematic of the etching results for the hexagonal graphene lattice and the corresponding orientation.  $a_1$ ,  $a_2$ , and  $a_3$  denote the axes in the basal plane. The black hexagon depicts an etched pit. Zigzag and armchair edges are illustrated. (b) SEM image of one square domain of graphene after etching, exhibiting a high density of hexagonal holes. The relationship between the domain shape and the graphene lattice is revealed. The grey wireframe refers to the domain shape, and the red wireframe refers to the etched pit. The scale bar represents 100 μm. (c) SEM image of a coalesced bicrystal after etching. The scale bar represents 20 μm. (d) and (e) Typical SEM images of etched hexagonal graphene pits taken from (c) for domains 1 and 2, respectively. The scale bar represents 2 μm. (f) Histogram of the relative twist angle of the etched hexagonal pits. Inset: a corresponding photograph of the graphene sample on Cu foil for the statistical analysis; the yellow boxes denote the areas for which data were collected.

of the as-obtained graphene bicrystals and their potential for practical applications.

Another concern about the graphene bicrystal growth is the absolute domain size, which is closely related to the density of 0°/30° GBs. The spatial priority of the nucleation on Cu foil is ascribed to its lower nucleation energy barrier [40, 41], which provides a clue for controlling the nucleation density. To reduce the amount of active sites, the removal of impurities and the smoothening of the surface of the Cu substrate are both fairly efficient [42, 43]. However, active sites such as Cu GBs inevitably remain, impeding the reduction of the nucleation numbers of graphene [23, 44]. A more efficient and controllable approach for suppressing the nucleation was applied, i.e., the introduction of an external compound onto

the Cu foil to intentionally passivate the active sites. We found that both annealing in the presence of a trace amount of O<sub>2</sub> and introducing a foreign passivating agent (triazine compounds) are able to efficiently reduce the nucleation density of graphene. In this regard, the lowest nucleation density was achieved by combining these two methods, i.e., using the cooperative passivation method. Different active sitepassivated growth strategies, such as growth without passivation, single passivation with only a trace amount of pre-oxidation, and cooperative passivation, were implemented to suppress the graphene nucleation (Fig. S7 in the ESM). Figures 3(a)-3(c) show SEM images of graphene domains grown by the three strategies. The cooperative passivation method shows a high efficiency for suppressing the nucleation density.

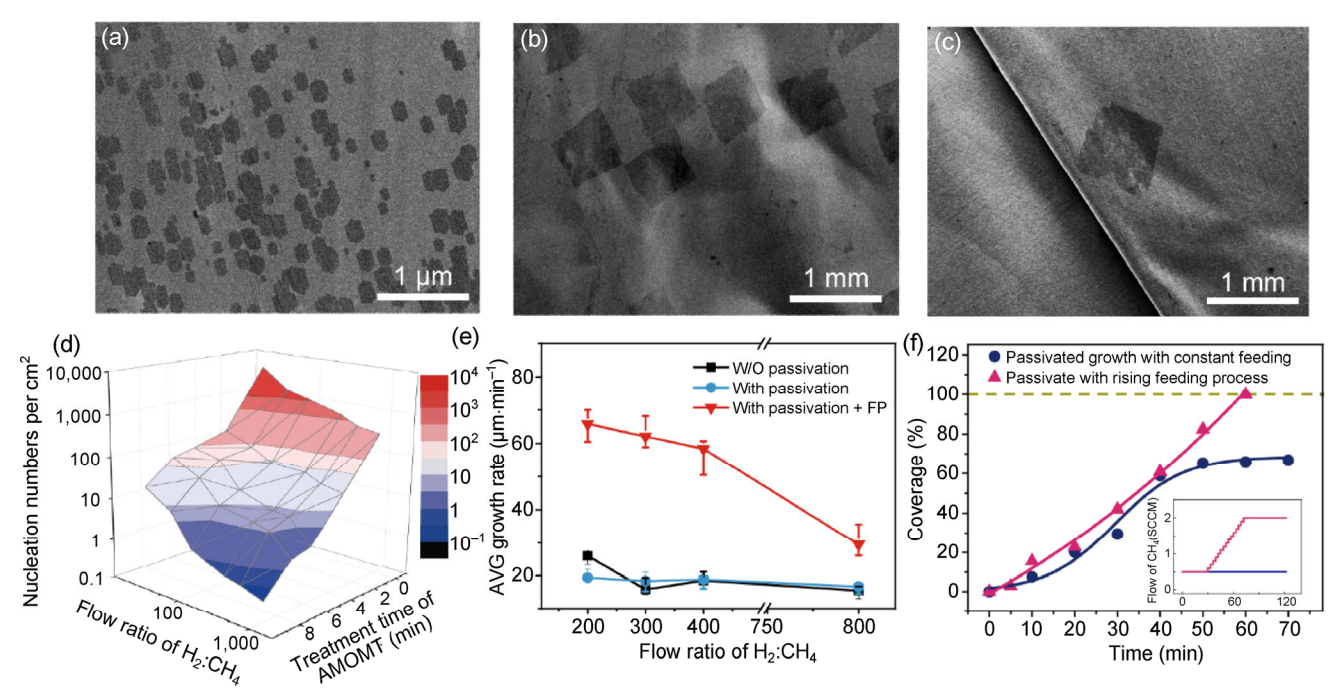


**Figure 3** Control of the nucleation density and growth rate of the bicrystals. (a)–(c) Typical SEM images of graphene with different nucleation densities. The graphene was grown without pretreatment (a), with a trace amount of pre-oxidation passivation pretreatment (b), and with cooperative passivation pretreatment (c). (d) Trend surface of graphene nucleation density with respect to the H<sub>2</sub>-to-CH<sub>4</sub> flow ratio and AMOMT pretreatment time. A smaller density is observed along the blue direction, and a larger density is observed along the red direction. (e) Growth rate of the graphene bicrystal with respect to the H<sub>2</sub>-to-CH<sub>4</sub> flow ratio, obtained by cooperative passivation graphene growth method with (red) and without (blue) the accelerated feeding process. For comparison, graphene was also grown without any treatment and accelerated feeding process (black). (f) Coverage of graphene on the Cu surface with respect to the growth time. The curves were obtained by fitting the experimental data for the cooperative passivation method with (rose red triangles) and without (blue dots) the accelerated feeding process. Inset: the temporal change of the methane (CH<sub>4</sub>) flow ratio in the accelerated feeding process.

Several triazine compounds, including melamine, 2,4diamino-6-methyl-1,3,5-triazine, and AMOMT were used as candidate compounds to passivate the active sites on the Cu foils through sublimation and transportation, before the initiation of the graphene growth. Among these compounds, AMOMT was the best choice for maintaining and even accelerating the growth. In a previous study [23], we realized the controlled growth of large single-crystal graphene, by using melamine—a type of triazine—as the active site-passivation compound and demonstrated that the deposition of triazine and the subsequent formation of C- and N-containing species at the Cu GBs reduced the nucleation density. The species selectively occupied the active sites and forced the graphene to nucleate on the flat Cu surface rather than at the Cu GBs, where the nucleation barrier was particularly high, yielding a suppressed nucleation density. To study the efficiency of passivation for controlling the nucleation density, the presence and release of the compounds in the entire growth process were confirmed via X-ray photoelectron spectroscopy, and the results were consistent with our previous results (Fig. S8 in the ESM).

The graphene nucleation was further suppressed by increasing the pretreatment time of the triazine derivative (AMOMT) and the  $H_2$ :CH<sub>4</sub> ratio (Fig. S9 in the ESM). The nucleation density was ~600 cm<sup>-2</sup> for growth without AMOMT pretreatment, whereas that for 9 min of pretreatment was reduced to ~0.57 cm<sup>-2</sup>. The nucleation density was highly dependent on the initial  $H_2$ :CH<sub>4</sub> ratios, as shown in Fig. 3(d). Detailed plots of the experimental results with respect to the pretreatment time and the  $H_2$ :CH<sub>4</sub> ratio are provided in Table S1 (in the ESM). The growth of sub-centimeter graphene single crystals was achieved by tuning the

pretreatment and growth parameters. For example, after 7 min of AMOMT pretreatment and the growth of graphene at a 500 H<sub>2</sub>:CH<sub>4</sub> ratio, the nucleation density was confined within a small range of 3–6 per square centimeter.

However, this approach reduced the growth rate because of the insufficient C supply. Obtaining a graphene domain ranging in size from nanometers to sub-centimeters usually takes 10 h. To overcome this problem, we gradually increased the precursor supply to increase the average growth rate of graphene in the absence of secondary nucleation. This is because after the initial nucleation stage, the C species preferred to attach to the present island edge rather than form a new cluster [24]. The drastic change in the C precursor may have enhanced the local concentration of the C species and thus the secondary nucleation (Fig. S10 in the ESM). As shown in Fig. 3(e), the average graphene growth rate obtained by gradually accelerating the feeding of the precursors was clearly higher than the growth rate with constant feeding, regardless of the C supply. The growth rate was unaffected by the external AMOMT passivation, indicating that AMOMT is a suitable choice for controlling the graphene nucleation. According to the model for the formation of graphene on Cu [45-47] the growth rate is determined by the amount of active C species produced on the Cu surface for the graphene growth. Because of the gradual reduction of the catalytic Cu surface during the growth, the amount of active C species becomes very limited, leading to a reduced growth rate and even the termination of the growth. To investigate the growth dynamics, the time evolution of the graphene coverage on the Cu was examined, as shown in Fig. 3(f). The results confirm the significant enhancement of the growth rate due to the accelerated feeding (for the data-processing details, see the ESM and Fig. S11 in the ESM). For graphene growth with a constant C supply, the graphene coverage increased almost linearly with respect to the growth time at the initiation stage but subsequently suffered from degradation [48], and the growth nearly stopped at 70% coverage. Consequently, the graphene did not form a continuous film (100% coverage). In contrast, with the programmed feeding, the growth rate exhibited no degradation throughout the entire growth process, confirming the effectiveness of our strategy.

Before the coalescence of the discrete arranged domains, each of the square graphene domains was a single crystal. To confirm the high quality of the as-formed square-shaped graphene, SAED patterns were collected for a millimeter-sized square domain transferred onto a TEM grid (the data-collection area is shown in the left inset of Fig. 4(a)). The histogram of the pattern orientation distributions extracted from the extensive SAED patterns shows pronounced peaks separated by a rotation of <1.2°, confirming the single-crystal nature of each separated square domain. As shown in Fig. S12 in the ESM, the SAED patterns remained practically unchanged with increasing distance, confirming the single-crystal lattice structure of the entire graphene domain. Aberration-corrected high-resolution TEM was performed to determine the atomic-resolution structure of the domain, as shown in Fig. 4(b), revealing a perfect C lattice having six-fold symmetry without structural defects or disorder. Raman spectroscopy was performed to further characterize the quality and uniformity of the graphene domains transferred onto the Si/SiO<sub>2</sub> substrate (Fig. S13 in the ESM). A series of spectra were obtained at random locations in one grain, as shown in Fig. 4(c). The integrated intensity of the 2D peak (2,670 cm<sup>-1</sup>) was more than twice as large as that of the G peak (1,585 cm<sup>-1</sup>), and the full-width at half-maximum of the 2D peak was ~33 cm<sup>-1</sup>, indicating the monolayer nature and high quality of the graphene domains [12, 49]. This high quality of the as-formed graphene was confirmed by the negligible D-band intensity.

The graphene bicrystal films were easily obtained by extending the growth time and transferred onto quartz and ethylene vinyl acetate/polyethylene terephthalate (EVA/PET) plastic film. The optical transmittance of the graphene on the quartz and EVA/PET was very high—approximately 97.7% and 95%, respectively— over a wide spectrum (400 to 2,000 nm), as shown in Fig. 4(d). The excellent conductivity (Fig. S15 in the ESM) and transmittance are very important for practical applications. To demonstrate the potential applications of the as-formed graphene film, Fig. 4(e) presents a temperature map of the surface of the graphene films transferred onto quartz (1.5 cm × 1.5 cm), which was supplied with a 15-V input voltage. The

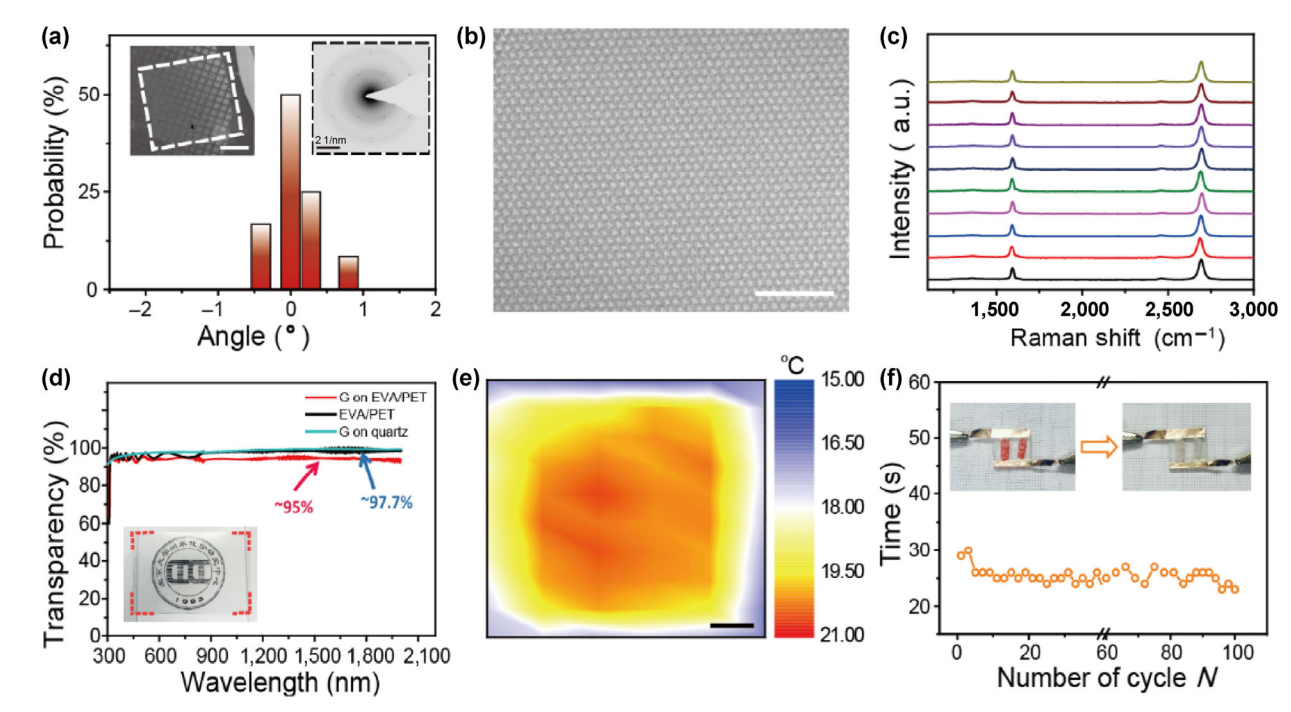


Figure 4 Characterization of the graphene bicrystal within the large domain and its film. (a) Histogram of the angle distribution from extensive SAED patterns for one graphene domain ~1.5 mm in size. Inset (left): an SEM image of this graphene domain transferred onto a C-film TEM grid. The scale bars represent 250 μm. Inset (right): a typical SAED pattern for the corresponding graphene domain. (b) Atomic-resolution TEM image of the graphene. The scale bar represents 2 nm. (c) Typical Raman spectra obtained for 10 random locations on the graphene, which are shown in Fig. S13 (in the ESM). (d) Ultraviolet–visible–near-infrared (UV–vis–NIR) spectra of continuous graphene films, exhibiting a flat spectrum over a broad wavelength range. Inset: photograph of a graphene film transferred onto PET/EVA. (e) Contour map of the surface temperature of a graphene film transferred onto 1.5 cm × 1.5 cm quartz glass at an input voltage of 15 V. The scale bar represents 2 mm. (f) Cycling performance of a thermochromic display made with three layers of graphene film/quartz glass at an input voltage of 15 V, indicating stable thermochromic behavior over 100 cycles. Inset: Photographs of the display before (left) and after (right) the voltage was applied.

surface temperature range was approximately 20 ± 0.5 °C (room temperature = 14.5 °C) in the central region, indicating the excellent uniformity of the graphene films [50]. Moreover, the highly uniform multilayer graphene film fabricated via the transfer methods also exhibited good heating performance (Fig. S16 in the ESM). The average equilibrium temperature increased with the applied power, which was tuned according to the input voltage (from 5 to 15 V). To exploit the outstanding electrical-heating performance of the graphene films, a series of heating devices were tested. Color-reversible thermochromic ink (color change: bright red to milky white) [51] with a ribbon shape was deposited on the three layers of graphene films transferred onto quartz (1.5 cm × 1.5 cm), and metal electrodes were placed at the edge of the graphene film/quartz. The color switching of the ink occurred at 31 °C. Complete color change induced by the heat was obtained within 25 s by applying a low direct-current voltage (15 V) to the device (inset in Fig. 4(f)). The average equilibrium temperature of the three-layer graphene film was ~48 °C, satisfying the demand for most types of commercial thermochromic ink (30–50 °C). There was no detectable deterioration, even after 100 cycles (Fig. 4(f)).

## 3 Conclusions

We demonstrated a facile strategy for the rapid growth of large-area angle-confined graphene bicrystals, which exhibited two lattice orientations with a tilt angle of ~30°. An efficient cooperative passivation strategy was developed to suppress the graphene nucleation density using a novel passivation compound. A rational precursor-feeding strategy was implemented to offset the insufficient C supply during the growth, yielding

a high growth rate of 70 μm·min<sup>-1</sup> for sub-centimeter graphene single crystals. A series of characterizations revealed the high quality of the as-obtained graphene bicrystals, which satisfy the demands of practical applications.

#### 4 Method

#### 4.1 Substrate pretreatment and graphene growth

Commercially available Cu foil (98% purity, 25 µm thick, Alfa Aesar) was electrochemically polished and cut into pieces. The foils were stacked and placed in the hot center of a furnace as a catalytic substrate. Then, 0.5 g of AMOMT was placed 30 cm upstream from the center, and the system was pumped to a base pressure of 0.1 Pa. Next, 200 sccm Ar was introduced into the system for ~15 min to blow the air out, followed by the re-pumping of the system to the base pressure (~1 Pa). A schematic of the experimental setup is shown in Fig. S17(a) (in the ESM). At the first stage, the flapper valve before the pump was closed, and the system was sealed until it was heated to 1,025 °C. Air containing O<sub>2</sub> was the remaining gas under the base pressure, and the O2 flow rate was calculated as ~0.1 sccm. After reaching 1,025 °C, the Cu foil continued to be annealed for 0.5 h, and then 100-200 sccm H<sub>2</sub> (90–180 Pa) was introduced into the system for 5–15 min to remove the adsorbed O on the surface of the Cu foil. Before the initiation of the growth, AMOMT powder was heated to 120 °C for gradual sublimation, and 100 sccm Ar was introduced for carrying the reagents downstream to the surface of the catalyst. Then, 0.5-3 sccm CH<sub>4</sub> and 50-500 sccm H<sub>2</sub> were introduced into the system and maintained for 10-60 min according to the request of the target samples. After the nucleation step, the feeding was gradually accelerated via the process represented in Fig. S17(b) (in the ESM). Finally, the sample was rapidly cooled to room temperature without changing the gas flow. Additional details regarding the catalytic substrate pretreatment and experiment are provided in the ESM.

#### 4.2 Characterization

OM images were obtained using an Olympus DX51 microscope. SEM characterizations were performed

using a Hitachi S-4800 with an acceleration voltage of 5–30 kV. Raman spectra were measured using a Jobin Yvon LabRAM HR 800UV with a 25-mW, 514.5-nm laser. SAED measurements were performed using an FEI Tecnai F30 with an acceleration voltage of 300 kV. Aberration-corrected high-resolution TEM was performed using an FEI 80–300 Environmental Titan operated in the monochromatic mode at 80 kV. The transmittance was measured using a UV-vis-NIR Perkin Elmer Lambda 950 spectrophotometer.

# Acknowledgements

We acknowledge financial support from the National Natural Science Foundation of China (Nos. 21173004, 51520105003, 51432002, 21222303 and 51362029) and the National Basic Research Program of China (Nos. 2014CB932500, 2013CB932603, 2012CB933404, 2011CB933003, and 2011CB921904), the National Program for Support of Top-Notch Young Professionals, and Beijing Municipal Science & Technology Commission (No. Z161100002116002).

Electronic Supplementary Material: Supplementary material (detailed experimental section, schematic of the fabrication process, SEM images, TEM image and so on) is available in the online version of this article at http://dx.doi.org/10.1007/s12274-017-1534-2.

### References

- Castro Neto, A. H.; Guinea, F.; Peres, N. M. R.; Novoselov, K. S.; Geim, A. K. The electronic properties of graphene. *Rev. Mod. Phys.* 2009, *81*, 109–162.
- [2] Addou, R.; Batzill, M. Defects and domain boundaries in self-assembled terephthalic acid (TPA) monolayers on CVD-grown graphene on Pt (111). *Langmuir* 2013, 29, 6354–6360.
- [3] Huang, P. Y.; Ruiz-Vargas, C. S.; van der Zande, A. M.; Whitney, W. S.; Levendorf, M. P.; Kevek, J. W.; Garg, S.; Alden, J. S.; Hustedt, C. J.; Zhu, Y. et al. Grains and grain boundaries in single-layer graphene atomic patchwork quilts. *Nature* 2011, 469, 389–392.
- [4] Duong, D. L.; Han, G. H.; Lee, S. M.; Gunes, F.; Kim, E. S.; Kim, S. T.; Kim, H.; Ta, Q. H.; So, K. P.; Yoon, S. J. et al. Probing graphene grain boundaries with optical microscopy. *Nature* **2012**, *490*, 235–239.

- [5] Lee, G.-H.; Cooper, R. C.; An, S. J.; Lee, S.; van der Zande, A.; Petrone, N.; Hammerberg, A. G.; Lee, C.; Crawford, B.; Oliver, W. High-strength chemical-vapor-deposited graphene and grain boundaries. *Science* 2013, 340, 1073–1076.
- [6] Carlsson, J. M.; Ghiringhelli, L. M.; Fasolino, A. Theory and hierarchical calculations of the structure and energetics of [0001] tilt grain boundaries in graphene. *Phys. Rev. B* 2011, 84, 165423.
- [7] Rasool, H. I.; Ophus, C.; Klug, W. S.; Zettl, A.; Gimzewski, J. K. Measurement of the intrinsic strength of crystalline and polycrystalline graphene. *Nat. Commun.* 2013, 4, 2811.
- [8] Zhang, X. Y.; Xu, Z. W.; Yuan, Q. H.; Xin, J.; Ding, F. The favourable large misorientation angle grain boundaries in graphene. *Nanoscale* 2015, 7, 20082–20088.
- [9] Yazyev, O. V.; Chen, Y. P. Polycrystalline graphene and other two-dimensional materials. *Nat. Nanotechnol.* 2014, 9, 755–767.
- [10] Wood, J. D.; Schmucker, S. W.; Lyons, A. S.; Pop, E.; Lyding, J. W. Effects of polycrystalline cu substrate on graphene growth by chemical vapor deposition. *Nano Lett.* 2011, 11, 4547–4554.
- [11] Kim, K.; Lee, Z.; Regan, W.; Kisielowski, C.; Crommie, M. F.; Zettl, A. Grain boundary mapping in polycrystalline graphene. ACS Nano 2011, 5, 2142–2146.
- [12] Li, X. S.; Cai, W. W.; An, J.; Kim, S.; Nah, J.; Yang, D. X.; Piner, R.; Velamakanni, A.; Jung, I.; Tutuc, E. et al. Largearea synthesis of high-quality and uniform graphene films on copper foils. *Science* 2009, 324, 1312–1314.
- [13] Lin, P.; Palumbo, G.; Harase, J.; Aust, K. T. Coincidence site lattice (CSL) grain boundaries and Goss texture development in Fe-3% Si alloy. *Acta Mater.* 1996, 44, 4677–4683.
- [14] Gertsman, V. Y.; Bruemmer, S. M. Study of grain boundary character along intergranular stress corrosion crack paths in austenitic alloys. *Acta Mater.* 2001, 49, 1589–1598.
- [15] Chun, H.; Na, S.-M.; Mudivarthi, C.; Flatau, A. B. The role of misorientation and coincident site lattice boundaries in Goss-textured Galfenol rolled sheet. J. Appl. Phys. 2010, 107, 09A960.
- [16] Saylor, D. M.; Rohrer, G. S. Measuring the influence of grain-boundary misorientation on thermal groove geometry in ceramic polycrystals. *J. Am. Ceram. Soc.* 1999, 82, 1529–1536.
- [17] Sato, Y.; Yamamoto, T.; Ikuhara, Y. Atomic structures and electrical properties of ZnO grain boundaries. *J. Am. Ceram. Soc.* **2007**, *90*, 337–357.
- [18] Todt, V. R.; Zhang, X. F.; Miller, D. J.; St. Louis-Weber, M.; Dravid, V. P. Controlled growth of bulk bicrystals and the investigation of microstructure-property relations of YBa<sub>2</sub>Cu<sub>3</sub>O<sub>x</sub> grain boundaries. *App. Phys. Lett.* **1996**, *69*, 3746–3748.

- [19] Fan, Z. X.; Huang, X.; Han, Y.; Bosman, M.; Wang, Q. X.; Zhu, Y. H.; Liu, Q.; Li, B.; Zeng, Z. Y.; Wu, J. et al. Surface modification-induced phase transformation of hexagonal close-packed gold square sheets. *Nat. Commun.* 2015, 6, 6571.
- [20] Yuan, Q. H.; Song, G. Y.; Sun, D. Y.; Ding, F. Formation of graphene grain boundaries on Cu(100) surface and a route towards their elimination in chemical vapor deposition growth. Sci. Rep. 2014, 4, 6541.
- [21] Wang, H.; Xu, X. Z.; Li, J. Y.; Lin, L.; Sun, L. Z.; Sun, X.; Zhao, S. L.; Tan, C. W.; Chen, C.; Dang, W. H. et al. Surface monocrystallization of copper foil for fast growth of large single-crystal graphene under free molecular flow. *Adv. Mater.* 2016, 28, 8968–8974.
- [22] Barrett, C. S.; Massalski, T. B. Structure of Metals; Pergamon: New York, 1980.
- [23] Lin, L.; Li, J. Y.; Ren, H. Y.; Koh, A. L.; Kang, N.; Peng, H. L.; Xu, H. Q.; Liu, Z. F. Surface engineering of copper foils for growing centimeter-sized single-crystalline graphene. *ACS Nano* 2016, 10, 2922–2929.
- [24] Lin, L.; Sun, L. Z.; Zhang, J. C.; Sun, J. Y.; Koh, A. L.; Peng, H. L.; Liu, Z. F. Rapid growth of large single-crystalline graphene via second passivation and multistage carbon supply. *Adv. Mater.* 2016, 28, 4671–4677.
- [25] Wu, T. R.; Zhang, X. F.; Yuan, Q. H.; Xue, J. C.; Lu, G. Y.; Liu, Z. H.; Wang, H. S.; Wang, H. M.; Ding, F.; Yu, Q. K. et al. Fast growth of inch-sized single-crystalline graphene from a controlled single nucleus on Cu-Ni alloys. *Nat. Mater.* 2016, 15, 43–47.
- [26] Lee, J.-H.; Lee, E. K.; Joo, W.-J.; Jang, Y.; Kim, B.-S.; Lim, J. Y.; Choi, S.-H.; Ahn, S. J.; Ahn, J. R.; Park, M.-H. et al. Wafer-scale growth of single-crystal monolayer graphene on reusable hydrogen-terminated germanium. *Science* 2014, 344, 286–289.
- [27] Nie, S.; Wofford, J. M.; Bartelt, N. C.; Dubon, O. D.; McCarty, K. F. Origin of the mosaicity in graphene grown on Cu(111). *Phys. Rev. B* 2011, 84, 155425.
- [28] Murdock, A. T.; Koos, A.; Britton, T. B.; Houben, L.; Batten, T.; Zhang, T.; Wilkinson, A. J.; Dunin-Borkowski, R. E.; Lekka, C. E.; Grobert, N. Controlling the orientation, edge geometry, and thickness of chemical vapor deposition graphene. ACS Nano 2013, 7, 1351–1359.
- [29] Merchant, H. D.; Liu, W. C.; Giannuzzi, L. A.; Morris, J. G. Grain structure of thin electrodeposited and rolled copper foils. *Mater. Charact.* 2004, 53, 335–360.
- [30] Wilson, N. R.; Marsden, A. J.; Saghir, M.; Bromley, C. J.; Schaub, R.; Costantini, G.; White, T. W.; Partridge, C.; Barinov, A.; Dudin, P. et al. Weak mismatch epitaxy and structural feedback in graphene growth on copper foil. *Nano Res.* 2013, 6, 99–112.

- [31] Chen, S. S.; Ji, H. X.; Chou, H.; Li, Q. Y.; Li, H. Y.; Suk, J. W.; Piner, R.; Liao, L.; Cai, W. W.; Ruoff, R. S. Millimeter-size single-crystal graphene by suppressing evaporative loss of Cu during low pressure chemical vapor deposition. *Adv. Mater.* 2013, 25, 2062–2065.
- [32] Rasool, H. I.; Song, E. B.; Mecklenburg, M.; Regan, B. C.; Wang, K. L.; Weiller, B. H.; Gimzewski, J. K. Atomic-scale characterization of graphene grown on copper (100) single crystals. J. Am. Chem. Soc. 2011, 133, 12536–12543.
- [33] Ogawa, Y.; Hu, B. S.; Orofeo, C. M.; Tsuji, M.; Ikeda, K.-I.; Mizuno, S.; Hibino, H.; Ago, H. Domain structure and boundary in single-layer graphene grown on Cu(111) and Cu(100) films. *J. Phys. Chem. Lett.* **2012**, *3*, 219–226.
- [34] Ma, T.; Ren, W. C.; Zhang, X. Y.; Liu, Z. B.; Gao, Y.; Yin, L.-C.; Ma, X.-L.; Ding, F.; Cheng, H.-M. Edge-controlled growth and kinetics of single-crystal graphene domains by chemical vapor deposition. *Proc. Natl. Acad. Sci. USA* 2013, 110, 20386–20391.
- [35] Girit, Ç. Ö.; Meyer, J. C.; Erni, R.; Rossell, M. D.; Kisielowski, C.; Yang, L.; Park, C.-H.; Crommie, M. F.; Cohen, M. L.; Louie, S. G. et al. Graphene at the edge: Stability and dynamics. Science 2009, 323, 1705–1708.
- [36] Yang, R.; Zhang, L. C.; Wang, Y.; Shi, Z. W.; Shi, D. X.; Gao, H. J.; Wang, E. G.; Zhang, G. Y. An anisotropic etching effect in the graphene basal plane. *Adv. Mater.* 2010, 22, 4014–4019.
- [37] Obraztsov, A. N.; Obraztsova, E. A.; Tyurnina, A. V.; Zolotukhin, A. A. Chemical vapor deposition of thin graphite films of nanometer thickness. *Carbon* 2007, 45, 2017–2021.
- [38] N'Diaye, A. T.; Van Gastel, R.; Martínez-Galera, A. J.; Coraux, J.; Hattab, H.; Wall, D.; Zu Heringdorf, F.-J. M.; Horn-von Hoegen, M.; Gómez-Rodríguez, J. M.; Poelsema, B. et al. *In situ* observation of stress relaxation in epitaxial graphene. *New J. Phys.* 2009, 11, 113056.
- [39] Nix, F. C.; MacNair, D. The thermal expansion of pure metals: Copper, gold, aluminum, nickel, and iron. *Phys. Rev.* **1941**, *60*, 597.
- [40] Chen, H.; Zhu, W. G.; Zhang, Z. Y. Contrasting behavior of carbon nucleation in the initial stages of graphene epitaxial growth on stepped metal surfaces. *Phys. Rev. Lett.* 2010, 104, 186101.
- [41] Yuan, Q. H.; Yakobson, B. I.; Ding, F. Edge-catalyst wetting and orientation control of graphene growth by chemical vapor

- deposition growth. J. Phys. Chem. Lett. 2014, 5, 3093-3099.
- [42] Mohsin, A.; Liu, L.; Liu, P. Z.; Deng, W.; Ivanov, I. N.; Li, G. L.; Dyck, O. E.; Duscher, G.; Dunlap, J. R.; Xiao, K. et al. Synthesis of millimeter-size hexagon-shaped graphene single crystals on resolidified copper. ACS Nano 2013, 7, 8924–8931.
- [43] Magnuson, C. W.; Kong, X. H.; Ji, H. X.; Tan, C.; Li, H. F.; Piner, R.; Ventrice, C. A.; Ruoff, R. S. Copper oxide as a "self-cleaning" substrate for graphene growth. *J. Mater. Res.* 2014, 29, 403–409.
- [44] Han, G. H.; Güneş, F.; Bae, J. J.; Kim, E. S.; Chae, S. J.; Shin, H.-J.; Choi, J.-Y.; Pribat, D.; Lee, Y. H. Influence of copper morphology in forming nucleation seeds for graphene growth. *Nano Lett.* 2011, 11, 4144–4148.
- [45] Kim, H.; Mattevi, C.; Calvo, M. R.; Oberg, J. C.; Artiglia, L.; Agnoli, S.; Hirjibehedin, C. F.; Chhowalla, M.; Saiz, E. Activation energy paths for graphene nucleation and growth on Cu. ACS Nano 2012, 6, 3614–3623.
- [46] Bhaviripudi, S.; Jia, X. T.; Dresselhaus, M. S.; Kong, J. Role of kinetic factors in chemical vapor deposition synthesis of uniform large area graphene using copper catalyst. *Nano Lett.* 2010, 10, 4128–4133.
- [47] Becker, O. M.; Ben-Shaul, A. Role and mechanism of island formation in chemisorption. *Phys. Rev. Lett.* **1988**, *61*, 2859–2862.
- [48] Li, X. S.; Magnuson, C. W.; Venugopal, A.; An, J.; Suk, J. W.; Han, B. Y.; Borysiak, M.; Cai, W. W.; Velamakanni, A.; Zhu, Y. W. et al. Graphene films with large domain size by a two-step chemical vapor deposition process. *Nano Lett.* 2010, 10, 4328–4334.
- [49] Ni, Z. H.; Wang, Y. Y.; Yu, T.; Shen, Z. X. Raman spectroscopy and imaging of graphene. *Nano Res.* **2008**, *1*, 273–291.
- [50] Sun, J. Y.; Chen, Y. B.; Priydarshi, M. K.; Chen, Z.; Bachmatiuk, A.; Zou, Z. Y.; Chen, Z. L.; Song, X. J.; Gao, Y. F.; Rümmeli, M. H. et al. Direct chemical vapor deposition-derived graphene glasses targeting wide ranged applications. *Nano Lett.* 2015, 15, 5846–5854.
- [51] Chen, Y. B.; Sun, J. Y.; Gao, J. F.; Du, F.; Han, Q.; Nie, Y. F.; Chen, Z. L.; Bachmatiuk, A.; Priydarshi, M. K.; Ma, D. L. et al. Growing uniform graphene disks and films on molten glass for heating devices and cell culture. *Adv. Mater.* 2015, 27, 7839–7846.